Available online at www.sciencedirect.com
ScienceDirect
Trans. Nonferrous Met. Soc. China 26(2016) 1063−1072
Transactions of Nonferrous Metals Society of China
www.tnmsc.cn

Polycrystal modeling of hot extrusion texture of AZ80 magnesium alloy

Yi-chuan SHAO, Tao TANG, Da-yong LI, Guo-wei ZHOU, Shao-rui ZHANG, Ying-hong PENG

State Key Laboratory of Mechanical System and Vibration, Department of Mechanical Engineering, Shanghai Jiao Tong University, Shanghai 200240, China

Received 10 April 2015; accepted 13 October 2015

Abstract: The visco-plastic self-consistent (VPSC) model is extended to take the dynamical recrystallization (DRX) into account so that the hot extrusion texture of AZ80 magnesium alloy can be properly modeled. The effects of extrusion temperatures and imposed boundary conditions on the resulting textures were investigated, and good agreement can be found between the simulated and the measured extrusion textures. The simulated results show that the DRX grains are responsible for the formation of the $\{2\bar{1}\bar{1}0\}$ fiber component since the $\{10\bar{1}0\}$ poles of the DRX grains are tilted away from those of the unrecrystallized grains during the formation of their high angle boundaries (HABs). Furthermore, the basal poles of the grains are favorably oriented to the transversal direction (TD) where the imposed deformation is larger due to lower slip resistance of the basal slip. The elevated temperature enhances the activity of pyramidal $\langle c+a \rangle$ slip modes and gives rise to a larger recrystallized volume fraction, resulting in a weakened extrusion texture.

Key words: AZ80 magnesium alloy; polycrystal plasticity; texture; hot forward extrusion; dynamic recrystallization

1 Introduction

Wrought magnesium alloys are able to offer higher potential of weight-savings than the aluminum alloys with excellent structure strength. Therefore, they have been increasingly utilized in automotive, aerospace and general engineering industries in recent decades. However, poor formability of the wrought magnesium alloys at room temperature still keeps them from wider use in manufacturing. By contrast, the wrought magnesium alloys respond more readily to the plastic deformation operated at elevated temperatures. Magnesium extrusion is one of the processing approaches which are well known for the workability optimization and the microstructure refinements of the products [1,2].

However, due to the low lattice symmetry and the limited slip systems of magnesium, the extruded magnesium alloys tend to exhibit strong textures which directly influence their mechanical properties and formability. Many experimental researches have been devoted to investigate the evolution of extrusion texture and its effects on the stress−strain behaviors of the extruded products [3,4]. In comparison with these experimental works, less numerical studies have been found to explore the evolution of the extrusion texture. Among all the modeling approaches, crystal plasticity models [5−9] are frequently adopted for texture simulation because of the use of slip system level constitutive laws. AGNEW et al [5] simulated the texture evolution during an equal channel angular extrusion (ECAE) process using a visco-plastic self-consistent (VPSC) model with simple shear boundary conditions imposed. Similarly, BISWAS et al [6] performed a VPSC simulation to investigate the extrusion textures of the extruded round rod and tube. MAYAMA et al [7] simulated the extrusion texture by implementing a crystal plasticity model into an approximate finite element model. These studies showed excellent capabilities of the crystal plasticity model in texture prediction, but with the attention mainly paid to the deformation textures of the original grains. In fact, modeling of the dynamical recrystallization (DRX) textures requires further investigation since DRX is liable to occur during hot extrusions. Some researchers [10,11] indicated that the recrystallized grains do not bring about significant change of the deformation texture. Based on this idea,

Foundation item: Project (311017) supported by the Major Projects of the Ministry of Education; Projects (51175335,51305261) supported by the National Natural Science Foundation of China; Project (2013M530194) supported by the Postdoctoral Science Foundation of China
Corresponding author: Da-yong LI; Tel/Fax: +86-21-34206313; E-mail: dyli@sjtu.edu.cn
DOI: 10.1016/S1003-6326(16)64203-6

WALDE and RIEDEDL [12] modeled the recrystallization texture of hot rolled AZ31 magnesium alloy with the assumption that all the recrystallized grains inherit their orientations from the parent grains. Although the dynamically recrystallized grains do not remarkably weaken the intensity of the basal texture, a misorientation angle was reported to develop between the deformation texture and the recrystallization texture [3,6,13]. This suggests that the initial orientations of the DRX nuclei may not be strictly the same as those of the parent grains during the deformation of magnesium alloys. The research of WU et al [14] on the ECAE of AZ31 magnesium alloy suggested that misorientation angles tend to develop between original grains and DRX grains around the $\langle 10\bar{1}0\rangle$ or $\langle 0001\rangle$ axis of the original grains as a result of multiple slip. OSTAPOVETS et al [15] incorporated a misorientation scheme into the VPSC model and justified the formation of misorientation angles around those two axes during the ECAE of AZ31 magnesium alloy.

The major objective of this work is to simulate the texture evolution of the AZ80 magnesium alloy during the hot forward extrusion. This is fulfilled using an extended VPSC model that considers the effects of dynamically recrystallized grains. It should be pointed out that the consideration of the DRX is simply confined to the contribution of the DRX grains to the overall deformation textures. Modeling the complete complexities of grain nucleation and growth is beyond the scope of this work.

2 Experimental

The wrought AZ80 magnesium alloy received under as-cast and homogenized condition was used throughout the present work. Hot compression tests were performed on the alloy at strain rates of 0.01, 0.1 and 1 s^{-1} over a temperature range of 573−673 K. All the samples were compressed to a maximum true strain of 1.0 and then quenched into water to preserve the microstructure in its as-deformed state.

Hot forward extrusion was carried out with an extrusion press, which is schematically illustrated in Fig. 1. A conical die with a die half angle θ=55° and a die hole with 15.5 mm in diameter was used in the extrusion. The as-cast billets with 60 mm in diameter were lubricated with MoS_2 paste, preheated to the extrusion temperature of 623 K and held for 1 h, and then put into the machine. The punch was set to move with a rate of 2 mm/s to press the billet through the die. An average strain rate of 0.92 s^{-1} can be reached under the given extrusion conditions. The extruded round rods were immediately quenched into water to prevent further microstructure evolution.

Crystallographic texture measurements of the extruded samples were carried out on the sections perpendicular to the extrusion direction. The bulk textures at the center of the extruded samples were measured via X-ray diffraction (XRD) with a Rigaku 2500PC X-ray diffractometer. Raw pole figures were collected up to a 70° sample tilt. LaboTex texture analysis software was used to generate orientation distributions and full pole figures.

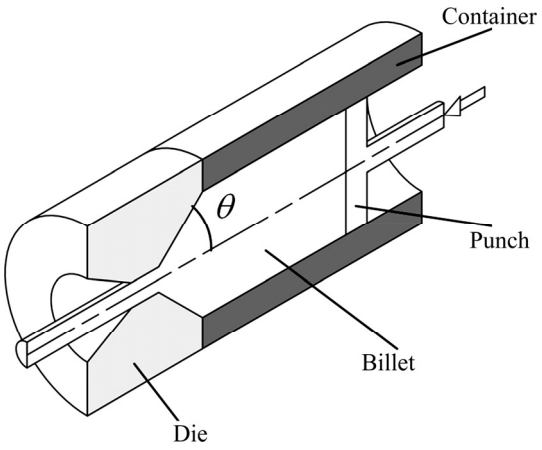

Fig. 1 Schematic drawing of hot forward extrusion process

3 Modeling procedures

3.1 Polycrystal modeling

The texture simulations are performed using a polycrystal model based on the VPSC framework proposed by LEBENSOHN and TOMÉ [16]. The polycrystal is represented as a collection of crystal orientations, and each single grain is treated as an ellipsoidal inclusion embedded within an infinite homogeneous effective medium (HEM) subjected to a uniform applied stress. The details of polycrystal framework can be found in Ref. [16].

The response of a single crystal can be written in a pseudo-linear form,

$$\dot{\varepsilon}_{ij}^{\mathrm{pl}}=\left\{\dot{\gamma}_0\sum_{s=1}^{S}\frac{m_{ij}^s m_{kl}^s}{\tau_c^s}\left(\frac{m_{pq}^s\sigma'_{pq}}{\tau_c^s}\right)^{n-1}\right\}\sigma'_{kl}=M_{ijkl}^{\mathrm{c(sec)}}\sigma'_{kl} \quad (1)$$

where $\dot{\varepsilon}^{\mathrm{pL}}$ is the plastic strain rate of the grain, $\dot{\gamma}_0$ is a reference rate, m_{ij}^s is the Schimd tensor for slip system (s), τ_c^s is the resolved shear stress on the system (s), $M_{ijkl}^{\mathrm{c(sec)}}$ is the secant visco-plastic compliance moduli of the grain, and σ'_{kl} is the deviatoric stress tensor in the grain.

Similarly, the macroscopic plastic strain rate $\dot{\boldsymbol{E}}^{\mathrm{pl}}$ can also be related to the macroscopic stress deviator $\boldsymbol{\Sigma}'$ by a secant visco-plastic compliance tensor $\boldsymbol{M}^{(\mathrm{sec})}$,

$$\dot{\boldsymbol{E}}^{\mathrm{pl}}=\boldsymbol{M}^{(\mathrm{sec})}\boldsymbol{\Sigma}' \quad (2)$$

Based on the Eshelby formalism for an ellipsoidal inclusion as proposed in Ref. [17], the relation between the macroscopic stress and the microscopic stress can be written as

$$\boldsymbol{\sigma}'=\boldsymbol{B}^{c}\sum' \tag{3}$$

where $\boldsymbol{B}^{c}$ is the accommodation tensor, which also relates the $\boldsymbol{M}^{c(sec)}$ to $\boldsymbol{M}^{(sec)}$ by

$$\boldsymbol{M}^{(sec)}=\langle\boldsymbol{M}^{c(sec)}\boldsymbol{B}^{c}\rangle \tag{4}$$

Given that the visco-plastic moduli of the grain and the HEM are unknown in advance, the self-consistency equation (Eq. (4)) and the stresses in each single grain have to be solved iteratively as prescribed in Ref. [16].

The predominant twin reorientation (PTR) scheme [18] is used to describe the contribution of twinning to the texture evolution. As prescribed in this scheme, for each single grain, c, the twinning shear, $\gamma_{t,c}$, accommodated by each twinning mode, t, and its associated volume fraction, $\varphi_{t,c}=\gamma_{t,c}/S_t$, is tracked throughout the deformation (where S_t is the reference shear of the twinning mode, t). The summation of the twinned volume fractions over all of the grains gives

$$\varphi_{\text{acc,mode}}=\sum_{c}\sum_{t}\frac{\gamma_{t,c}}{S_t} \tag{5}$$

At every incremental step, the accumulated twinned volume fraction of the predominant twinning system is compared against a dynamic threshold to decide whether reorientation occurs at current grain. If so, the entire grain is reoriented to a new orientation and this grain is included as the effective twinned fraction, $\varphi_{\text{eff,mode}}$.

A Voce type hardening law [19] is used to model the hardening behavior of each individual deformation mechanism within each individual grain, which is given by

$$\tau^{(\alpha)}=\tau_0^{(\alpha)}+(\tau_1^{(\alpha)}+\theta_1\gamma)\left\{1-\exp\left(-\frac{\theta_0\gamma}{\tau_1^{(\alpha)}}\right)\right\} \tag{6}$$

where τ_0 and τ_1 are the initial and back-extrapolated increase in the threshold stress, respectively, and θ_0 and θ_1 are the initial and final slopes of the hardening curve. These four parameters constitute the fitting parameters for each individual deformation mode.

Allowing for latent hardening effects, the hardening for each mode is accomplished by the following equation at the end of each incremental step:

$$\Delta\tau^{(\alpha)}=\frac{\mathrm{d}\tau^{(\alpha)}}{\mathrm{d}\gamma}\sum_{\beta}h^{\alpha\beta}\Delta\gamma^{\beta} \tag{7}$$

In other words, the incremental increase in the CRSS of the slip system α, $\Delta\tau^{(\alpha)}$, depends on the amount of shear strain accumulated by each slip system β. The latent hardening matrix, $h^{\alpha\beta}$, allows the strength of interaction between different slip systems to be modeled. Since twin boundaries are regarded as barriers to subsequent slip and twinning, the difference between slip−slip interactions and slip−twin interactions is described by the values of matrix $h^{\alpha\beta}$. All the elements of $h^{\alpha\beta}$ are set to 1 except if β is a twinning mode, in which case, $h^{\alpha\beta}$ is set to 1.8 [12].

Texture simulations are conducted on polycrystal aggregate of 1000 discrete orientations representative of the initial texture. Random starting texture is assumed for the as-cast alloy, which has been justified in Refs. [6,7]. The simple compression process is simulated by simply defining the velocity gradient $\boldsymbol{L}$ as

$$\boldsymbol{L}_{ij}=\dot{\varepsilon}\begin{bmatrix}0.5 & 0 & 0\\ 0 & 0.5 & 0\\ 0 & 0 & -1\end{bmatrix} \tag{8}$$

where $\dot{\varepsilon}$ is the strain rate and the component along the compression direction is labeled as $\boldsymbol{L}_{33}$. Similarly, the overall boundary condition of the extrusion process can be approximated by defining the velocity gradient $\boldsymbol{L}$ as

$$\boldsymbol{L}_{ij}=\begin{bmatrix}-0.5\dot{\varepsilon} & \dot{\varepsilon}_{12} & \dot{\varepsilon}_{13}\\ \dot{\varepsilon}_{21} & -0.5\dot{\varepsilon} & \dot{\varepsilon}_{23}\\ \dot{\varepsilon}_{31} & \dot{\varepsilon}_{32} & \dot{\varepsilon}\end{bmatrix} \tag{9}$$

where the component along the extrusion direction is labeled as $\boldsymbol{L}_{33}$. The shear components $\dot{\varepsilon}_{ij}$ $(i\neq j)$ are caused by the difference of material flow speed in the extruded billet. For the material located in the center of the extruded billet, the extrusion can be approximated by an equi-biaxial compression process in which case all the shear components in Eq. (9) are set to zero [6].

3.2 Consideration of DRX texture

Continuous dynamic recrystallization (CDRX) and discontinuous dynamic recrystallization (DDRX) are the dominant mechanisms for the recrystallization in hot deformation of wrought magnesium alloys in temperature range of 573−673 K [20]. The grain boundaries of new grains form either by the migration of existing grain boundaries or the continuous transformation of low-angle grain boundaries (LAGBs) to high-angle grain boundaries (HAGBs). As a result, the old grains are gradually replaced with a growing number of DRX grains. By virtue of the VPSC framework, the DRX grains are treated as a new set of ellipsoidal inclusions embedded into the HEM, and used as contributors to the overall texture and flow behavior of the polycrystal. The basal poles of the DRX grains are initially kept aligned to those of the parent grains which gives that the DRX do not weaken the orientation intensity of the overall basal texture [6]. However, a misorientation angle around ⟨0001⟩ axis between deformation and recrystallization textures was reported

in experimental studies on the magnesium extrusion textures [3,13]. SHAO et al [21] conducted a numerical test on the misorientation angle between the recrystallized and unrecrystallized grains and found that the lattice rotation around the *c*-axis during the formation of new grains results in the $\{11\bar{2}0\}$ extrusion fiber. Based on these findings, the new grains are initially rotated by an angle about the *c*-axis of their parent grains before they are plastically deformed. This misorientation angle is set to a random value higher than 15°, the conventional value of the misorientation of the HAGB.

The total recrystallized volume fraction throughout the deformation is controlled by an Avrami type equation [22], as given by

$$X_{\mathrm{drx}} = 1-\exp\left\{-\left[\left(\frac{\varepsilon-\varepsilon_{\mathrm{c}}}{\varepsilon_{\mathrm{s}}}\right)^{m}\right]\right\} \tag{10}$$

where X_{drx} is the accumulated recrystallized fraction at current step, m is treated as fitting parameters to control the increment of X_{drx} between two successive straining steps, ε_{c} and ε_{s} are the critical strain and the saturation strain, respectively. The former is typically known as the onset strain of the DRX, and the latter indicates a saturation of the softening caused by the DRX [23].

Detailed steps for the numerical implementation of DRX texture within the VPSC framework are as follows:

1) For an arbitrary straining step, either an unrecrystallized grain or a recrystallized grain can serve as the parent grain for a new grain. Detect whether the strain within the parent grain is larger than the critical strain, ε_{c}. The birth of new grains is not permitted if this condition is not satisfied.

2) Calculate the percentage increase of the recrystallized volume fraction and nucleation number of new grains for current step using Eq. (10).

3) Assign properties to each new DRX grains, including crystallographic orientations and hardening features. Orientation of a new grain is partly inherited from its parent grain according to the aforementioned assumption. The newly generated DRX grains are assumed to be stress-free and within the boundaries, therefore, the CRSS values of them are set to the original CRSS values of the parent grains.

4) Perform the VPSC algorithm while taking the new DRX grains into account. Update the stress and move on to the next straining step once the convergence of iteration was reached.

4 Results and discussion

4.1 Stress−strain behavior of as-cast alloy

As shown in the stress−strain curves in Fig. 2, the softening effect caused by DRX acts as a competitor of

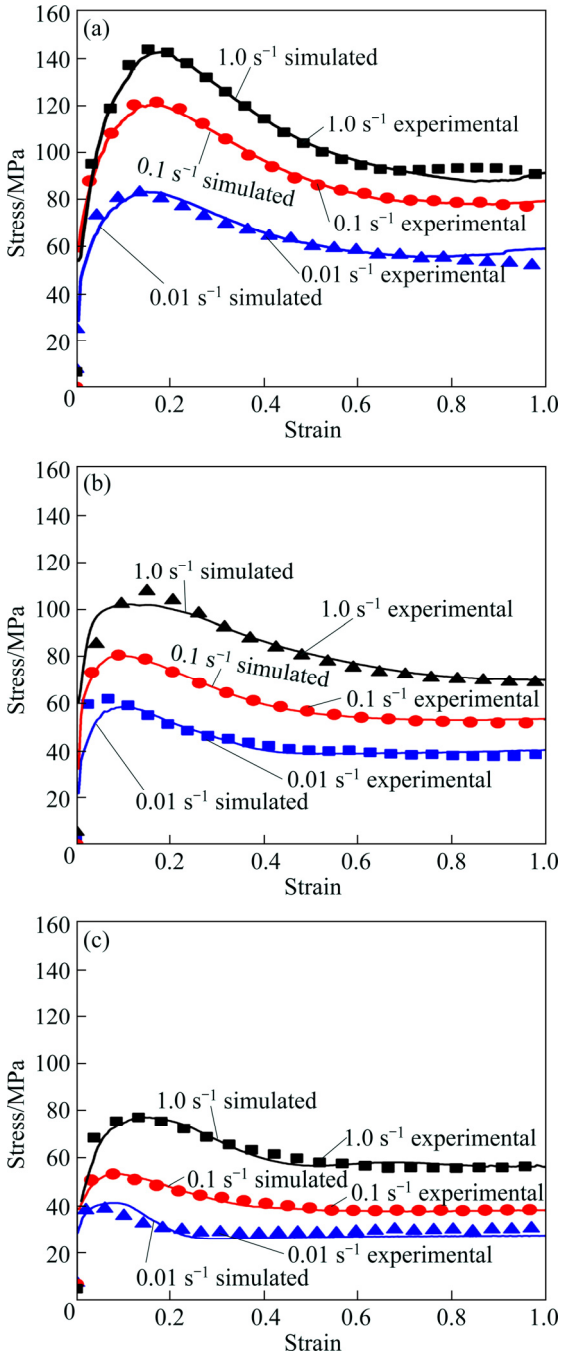

Fig. 2 Comparison of simulated (solid line) and measured stress−strain curves (symbol) of as-cast AZ80 magnesium alloy compressed at temperatures of 573 K (a), 623 K (b) and 673 K (c)

work hardening during the deformation at high temperatures. During the first few percent of the deformation, the work hardening predominates the deformation. It is then gradually suppressed by the softening effect caused by DRX as the deformation proceeds. An inflection point can be identified on the $\theta-\sigma$ curve (where the work hardening rate $\theta=\mathrm{d}\sigma/\mathrm{d}\varepsilon$), and is known as the onset of dynamic recrystallization (known as the critical strain, ε_{c}) [23]. Table 1 gives the

identified values of the critical strains, which are determined by solving $(\partial/\partial\sigma)(-\partial\theta/\partial\sigma)=0$. The flow stress decreases at a rate that declines with increasing the strain after the peak strain is exceeded. Thus, there exists a point on the flow curve where the hardening rate reaches a minimum and the softening effects tend to become saturated. This point can be obtained from $\partial\theta/\partial\varepsilon=0$, and referred to as saturation strain (ε_s) in Table 1. According to the study of QUAN et al [22], $\ln\varepsilon_c$ and $\ln\varepsilon_s$ can be linearly related to the logarithm of Zener−Hollomon parameter ($Z=\dot{\varepsilon}\exp[Q/(RT)]$, as given in Table 2.

Table 1 Peak stains, critical strains, and saturation strains determined at different strain rates and temperatures

Strain rate/s^{-1}	Peak strain			Critical strain			Saturation strain		
	573 K	623 K	673 K	573 K	623 K	673 K	573 K	623 K	673 K
0.01	0.130	0.051	0.044	0.068	0.027	0.023	0.236	0.156	0.076
0.1	0.173	0.104	0.061	0.062	0.059	0.024	0.261	0.194	0.130
1	0.161	0.158	0.132	0.050	0.037	0.032	0.290	0.238	0.235

4.2 Determination of material parameters

The deformation modes include basal ⟨*a*⟩ slip, prismatic ⟨*a*⟩ slip, pyramidal ⟨*c*+*a*⟩ slip and extension twinning. Hence, the fitting parameters at a given temperature include 16 Voce parameters (4 parameters per slip/twin system) and 1 DRX parameter. The trial-and-error methodology would be time-costing by simply refining the parameters and fitting the simulated flow curves to the experimental results. A fitting strategy is therefore proposed here for better efficiency.

The initial threshold stresses, τ_0, for the basal ⟨*a*⟩ slip and extension twin are athermal parameters [24], which remain unchanged at different temperatures. The values of τ_0 for the thermally activated systems, i.e., prismatic ⟨*a*⟩ slip system and pyramidal ⟨*c*+*a*⟩ slip system, follow a logarithmic stress law [25] given by

$$\tau=\alpha\ln Z-\beta \tag{11}$$

where α and β are the parameters. Considering the temperature range, the slip resistance stress is assumed to be linearly related to the temperatures. Practically, for the prismatic ⟨*a*⟩ slip and pyramidal ⟨*c*+*a*⟩ slip, the τ_0 and τ_1 at 623 and 673 K are progressively reduced from their best-fit counterparts at 573 K with increasing the temperature. Common difference between the slip resistance values for each two sequential temperatures is adjusted to best match the experimental flow curves.

On the other hand, the parameter m in the Avrami-type equation can be related to the Zener−Hollomon parameter [26] by

$$m=K\exp\left(N\sqrt{\frac{Z}{A}}\right) \tag{12}$$

where K and N are the parameters that are optimized to better match the softening behavior of the experimental stress−strain curves at 573, 623 and 673 K, Z is the Zener-Hollomon parameter, and A is a material constant. The flow curves for different strain rates are directly simulated without fitting owing to the use of the visco-plastic law (Eq. (1)) with a rate sensitivity parameter of n=0.05. The simulated peak stresses shown in Fig. 2 reflect the effect of this visco-plastic law.

All the determined DRX parameters and Voce parameters are presented in Tables 2 and 3, respectively. Although several simulated flow curves in Fig. 2 do not exactly match the experimental ones, the strategy used here relies less on fitting and captures the main features of the stress−strain behaviors of the alloy.

Table 2 Best-fit DRX parameters for describing softening behavior of AZ80 magnesium alloy

Z	A	$\ln\varepsilon_c$
$\dot{\varepsilon}\exp[(2.24\times10^5)/(8.31T)]$	3.57×10^{17}	$0.0897\ln(Z/A)-3.3076$
$\ln\varepsilon_s$		m
$0.1111\ln(Z/A)-1.7850$		$1.1138\exp(0.0229\sqrt{Z/A})$

Table 3 Best-fit Voce parameters for describing hardening behavior of AZ80 magnesium alloy at different temperatures

Temperature/K	Deformation mode	Voce parameter/MPa			
		τ_0	τ_1	θ_0	θ_1
573	Basal ⟨*a*⟩ slip	3	3	20	0.001
	Prismatic ⟨*a*⟩ slip	17	14	40	0.001
	Pyramidal ⟨*c*+*a*⟩ slip	22	22	50	0.001
	Extension twinning	6	0	30	30
623	Basal ⟨*a*⟩ slip	3	2.5	20	0.001
	Prismatic ⟨*a*⟩ slip	12	10.5	40	0.001
	Pyramidal ⟨*c*+*a*⟩ slip	15	16.5	50	0.001
	Extension twinning	6	0	30	30
673	Basal ⟨*a*⟩ slip	3	2	20	0.001
	Prismatic	7	7	40	0.001
	Pyramidal ⟨*c*+*a*⟩ slip	8	11	50	0.001
	Extension twinning	6	0	30	30

4.3 Experimental verification of predicted extrusion texture

The texture of the extrusion process mentioned in Section 2 is predicted by performing the polycrystal simulation using the material parameters determined in Section 4.2. The comparison between the simulated textures and measured results is shown in Fig. 3. In particular, the simulated overall texture is split into the textures of the unrecrystallized grains and that of the DRX grains presented in the form of pole figures and ODF sections.

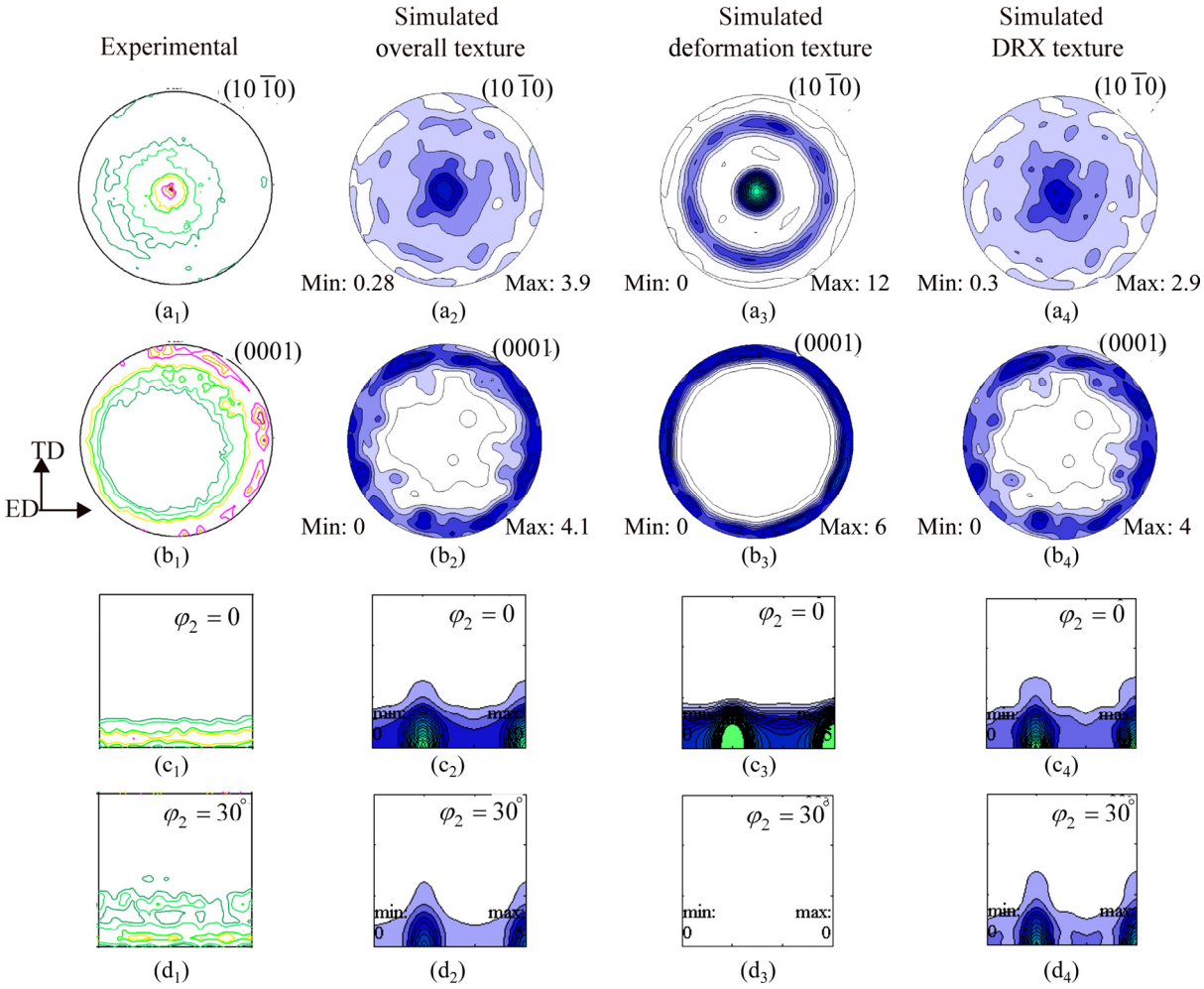

Fig. 3 Comparison of measured and simulated textures in terms of pole figures (a_1−b_4) and ODF sections (c_1−d_4) (simulated overall texture is split into deformation texture of unrecrystallized grains and recrystallization texture of DRX grains)

The predicted textures show that the basal planes of the grains are preferentially oriented parallel to the extrusion axis. As a result, a ring texture forms in the (0001) pole figure in which the intensity of the basal poles is essentially uniform along its perimeter. The prismatic $\langle 10\bar{1}0 \rangle$ poles of the grains are aligned with the extrusion axis to form a central dot encircled by a ring. This corresponds to the texture intensity at the ODF section φ_2=0. A secondary fiber component around the $\langle 2\bar{1}\bar{1}0 \rangle$ ||ED can be observed at the ODF section φ_2=30°. These simulated features are in good accordance with the measured results. The assumption regarding the initial orientations of the DRX grains proposed in Section 3.2 can therefore be justified.

The separation of overall extrusion textures offers a clear insight into the contribution of the unrecrystallized grains and the DRX grains, respectively. As shown in the ODF sections, the unrecrystallized grains are only responsible for the single fiber component around $\langle 10\bar{1}0 \rangle$ || ED (ODF section φ_2=0). Similar result has been reported in the simulation of BISWAS et al [6] which reproduced this type of fiber texture by considering the unrecrystallized grains only. In comparison, the DRX grains develop a secondary fiber component around the $\langle 2\bar{1}\bar{1}0 \rangle$ || ED (ODF section φ_2=30°) in addition to the primary fiber around $\langle 10\bar{1}0 \rangle$ || ED.

The formation of the extrusion texture of the AZ80 magnesium alloy can now be explained from a simulation viewpoint. During the extrusion, the unrecrystallized grains would be oriented to the primary stable orientation around $\langle 10\bar{1}0 \rangle$ || ED, in which case the grain rotations caused by two equivalent prismatic slip are canceled out [7]. The tendency for the new DRX grains oriented toward this stable orientation is reduced due to the lattice rotations caused by the recrystallization. During the formation of a new grain, it will tilt its prismatic planes away from those of the parent grains according to the assumption prescribed in Section 3.2. This contributes to the weakening of the orientation intensity of the prismatic $\langle 10\bar{1}0 \rangle$ poles and the presence of texture components at ODF section φ_2=30°.

4.4 Effects of imposed strain boundary conditions on extrusion textures

The effect of the strain components is investigated in order to better understand how the grain orientations respond to the boundary conditions of the extrusion. The polycrystal simulation of extrusion texture is performed to a final true strain of 1.0 with the relative values of L_{11}:L_{22}:L_{33} taken to be −0.6:−0.4:1, −0.7:−0.3:1, −0.8:−0.2:1 and −0.9:−0.1:1. In so doing, textures produced by different types of extrusion process at 623 K are simulated.

Figure 4 shows the resulting texture simulated with different relative values of L_{11}:L_{22}:L_{33}. It is observed that the symmetry of the texture evolves with the relative values of the strain components imposed on the polycrystal. A nearly radial symmetry can still be observed in the texture simulated with L_{11}:L_{22}=−0.6:−0.4. As the relative values of L_{11}:L_{22} increase from −0.7:−0.3 to −0.8:−0.2, the grains tend to tilt their basal poles toward the transversal direction where larger strain is imposed (TD_1 in Fig. 4). This tendency becomes even greater when L_{11}:L_{22} is taken to be −0.9:−0.1, in which case the ring-shaped texture vanishes.

The slip activities shown in Fig. 4 explain the texture evolution with changing the boundary conditions. In the four types of extrusion processes, the combination of the basal ⟨*a*⟩ slip and prismatic ⟨*a*⟩ slip dominates the plastic deformation. At the early stage of the

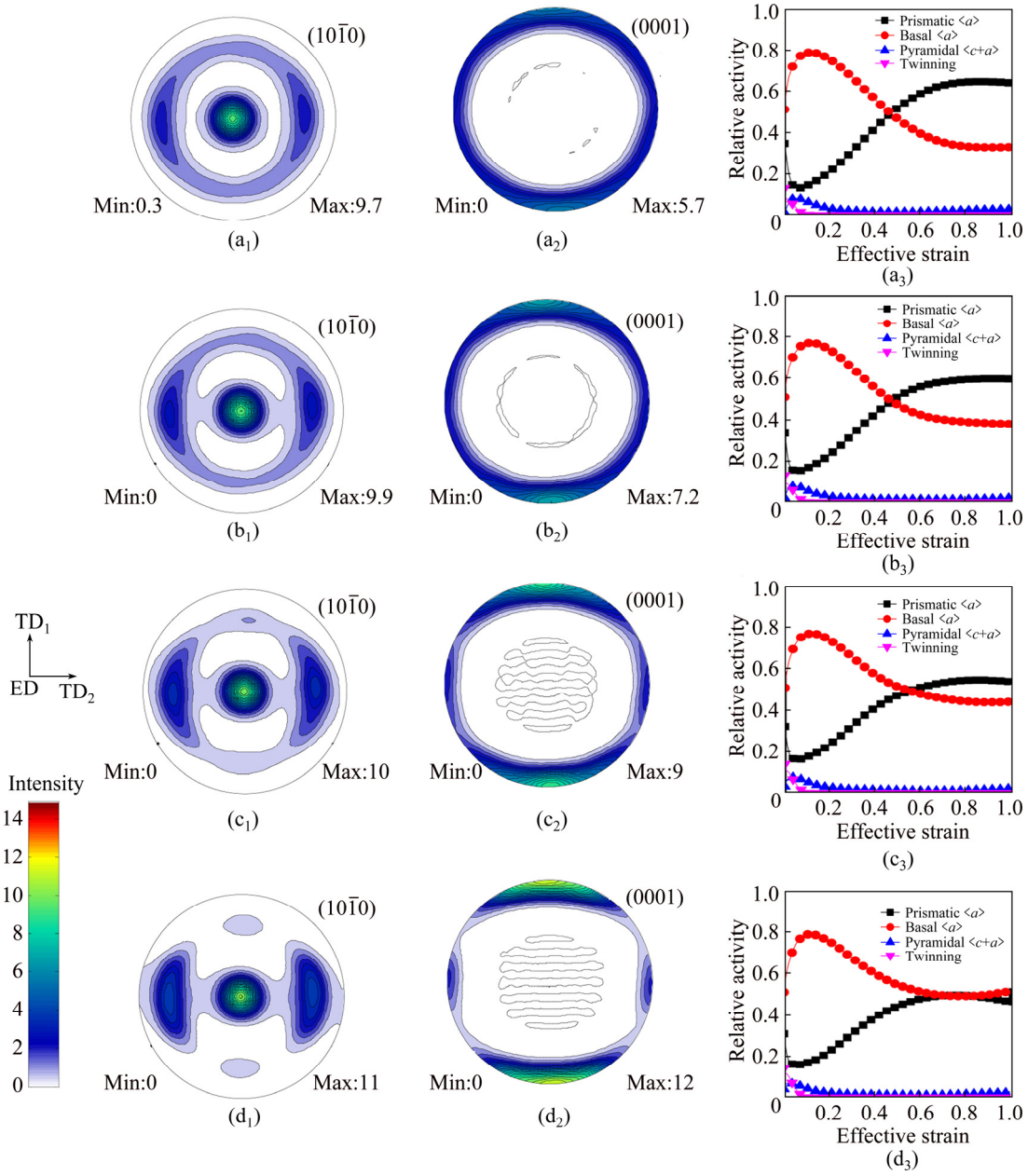

Fig. 4 Simulated textures and calculated activity of slip systems under different boundary conditions of extrusion with relative values L_{11}:L_{22}:L_{33} of −0.6:−0.4:1.0 (a_1−a_3), −0.7:−0.3:1.0 (b_1−b_3), −0.8:−0.2:1.0 (c_1−c_3) and −0.9:−0.1:1.0 (d_1−d_3)

deformation, the basal slip takes the priority over the prismatic slip owing to the lowest slip resistance. The grains rotate their basal pole toward the transversal direction as a result of the basal slip. However, the Schmid factor becomes lower as the angle between the basal pole and transversal direction gets smaller, resulting in the declining of the basal slip activity. On the contrary, the material flow facilitates the prismatic slip and enhances its activity as the prismatic slip becomes collinear with the extrusion direction.

In addition, an increase of the activity of the basal slip can be observed as the relative value of L_{11}:L_{22} increases from −0.6:−0.4 to −0.9:−0.1. The grains have to tilt their basal poles toward the axis in which the imposed strain is larger in order to accommodate the deformation. However, the prismatic slip is not responsible for the reorientation of the basal poles since the deformation caused by this kind of slip is the grain rotations around the *c*-axis. Although the pyramidal slip can also reorient the basal poles, the activation of this slip system is much harder than that of the basal slip. Therefore, the basal slip has to compensate the deformation needed to rotate the basal poles to the axis in which the imposed strain is larger.

4.5 Effects of extrusion temperatures on deformation modes and textures

The simulated $(10\bar{1}0)$ and (0001) pole figures of the extrusion texture at three different temperatures are shown in Fig. 5, along with the calculated activities of

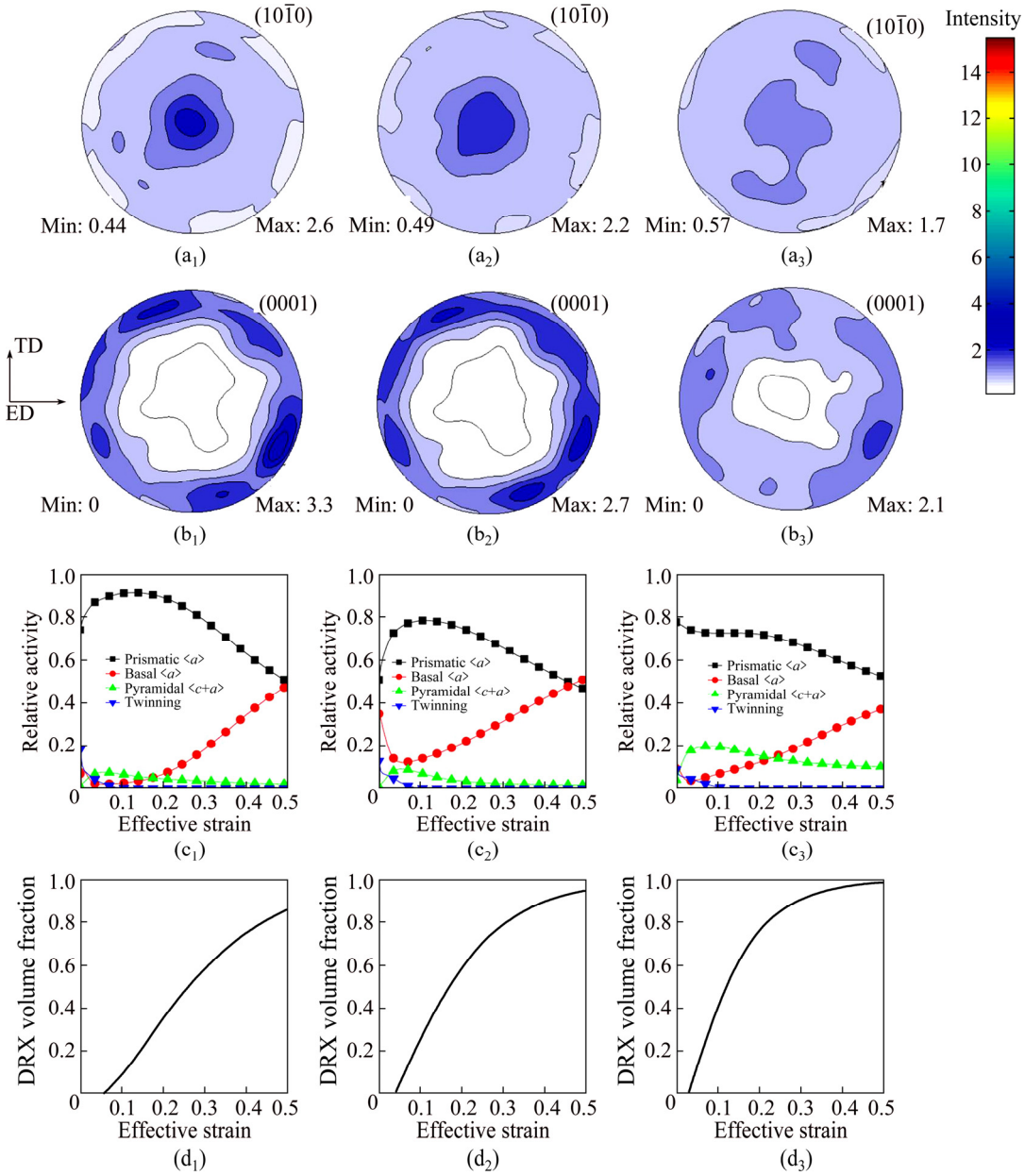

Fig. 5 Simulated extrusion textures (ε=0.5) shown by $(10\bar{1}0)$ (a_1−a_3) and (0001) (b_1−b_3) pole figures, relative activity of deformation modes corresponding to simulated textures (c_1−c_3), and recrystallized volume fraction as function of effective strain during extrusion (d_1−d_3) at temperatures of 573 K (a_1, b_1, c_1, d_1), 623 K (a_2, b_2, c_2, d_2) and 673 K (a_3, b_3, c_3, d_3)

the slip/twin modes and the evolution of the recrystallized volume fraction during the extrusion process.

As shown in Figs. 5(a_1−b_3), the angular spread of the basal poles in the simulated pole figures becomes greater when the extrusion temperatures increase from 573 to 673 K. This can be explained from three different aspects. First, the decreasing rate of the basal slip activity becomes lower with increasing the temperature, leading to a slower reorientation of the basal poles of the grains. Hence, at higher temperatures, more grains are left at positions with larger angles between the basal poles and the transversal direction.

Furthermore, as the temperature increases, the pyramidal ⟨*c*+*a*⟩ slip becomes easier to be activated and is enabled to accommodate a greater share of plastic deformation. This can be viewed as another contributor to the weakened basal textures. As reported in Refs. [27,28], the typical effects of the enhanced pyramidal ⟨*c*+*a*⟩ slip on the extrusion texture include texture gradient and off-basal texture components.

Last, the elevated temperature affects the recrystallized volume fraction and the texture. As shown in Table 2, both the critical strain and the saturation strain become smaller with increasing the temperature, which results in an earlier onset and a quicker saturation of the dynamic recrystallization. As shown in Figs. 5(d_1−d_3), the accumulated recrystallized volume fraction during extrusion at 573 K reaches 80% after the imposed strain is larger than 0.4. The required strain for reaching such a recrystallized fraction decreases to 0.3 at 623 K. The recrystallized volume fraction increases even faster at 673 K in which case a total fraction of 80% is reached when the imposed strain is about 0.2. The reorientation of the DRX grains is slower than that of the unrecrystallized grains due to lower levels of stress and shear strain within those new grains. Therefore, the angular spread of the basal poles of the DRX grains is greater than that of the original grains. This contributes to a weaker overall texture when the volume fraction of DRX grains increases with increasing the temperature.

5 Conclusions

1) The simulated extrusion textures show that the formation of fiber texture component around $\langle 2\bar{1}\bar{1}0\rangle \parallel$ ED can be attributed to the DRX grains. The unrecrystallized grains are only responsible for the orientation intensity around $\langle 10\bar{1}0\rangle \parallel$ ED. It can be deduced that the misorientation between the deformation texture and the recrystallization texture results from the lattice rotation during the formation of the DRX grains.

2) The deformation mechanism of the alloy is affected by the boundary condition imposed on the extruded material. The basal poles of the grains are favorably oriented toward the transversal direction where the largest plastic strain is imposed. This tendency becomes greater when the difference between the imposed strains in the two transversal axes increases.

3) The simulated results show that the elevated extrusion temperature contributes to a greater angular spread of the basal poles. This can be attributed to the enhanced activity of basal slip and pyramidal slip and the increased recrystallized volume fraction as a result of the elevated extrusion temperature.

References

[1] GALL S, MÜLLER S, REIMERS W. Microstructure and mechanical properties of magnesium AZ31 sheets produced by extrusion [J]. International Journal of Material Forming, 2013, 6(1): 187−197.

[2] SHAHZAD M, WAGNER L. Influence of extrusion parameters on microstructure and texture developments, and their effects on mechanical properties of the magnesium alloy AZ80 [J]. Materials Science and Engineering A, 2009, 506(1): 141−147.

[3] BOHLEN J, YI S, LETZIG D, KAINER K U. Effect of rare earth elements on the microstructure and texture development in magnesium–manganese alloys during extrusion [J]. Materials Science and Engineering A, 2010, 527(26): 7092−7098.

[4] STANFORD N, BARNETT M R. The origin of “rare earth” texture development in extruded Mg-based alloys and its effect on tensile ductility [J]. Materials Science and Engineering A, 2008, 496(1): 399−408.

[5] AGNEW S R, MEHROTRA P, LILLO T M, STOICA G M, LIAW P K. Texture evolution of five wrought magnesium alloys during route A equal channel angular extrusion: Experiments and simulations [J]. Acta Materialia, 2005, 53(11): 3135−3146.

[6] BISWAS S, SUWAS S, SIKAND R, GUPTA A K. Analysis of texture evolution in pure magnesium and the magnesium alloy AM30 during rod and tube extrusion [J]. Materials Science and Engineering A, 2011, 528(10): 3722−3729.

[7] MAYAMA T, NODA M, CHIBA R, KURODA M. Crystal plasticity analysis of texture development in magnesium alloy during extrusion [J]. International Journal of Plasticity, 2011, 27(12): 1916−1935.

[8] HUANG Shi-yao, ZHANG Shao-rui, LI Da-yong, PENG Ying-hong. Modeling texture evolution during rolling process of AZ31 magnesium alloy with elasto-plastic self consistent model [J]. Transactions of Nonferrous Metals Society of China, 2011, 21(6): 1348−1354.

[9] HUANG Shi-yao, ZHANG Shao-rui, LI Da-yong, PENG Ying-hong. Simulation of texture evolution during plastic deformation of FCC, BCC and HCP structured crystals with crystal plasticity based finite element method [J]. Transactions of Nonferrous Metals Society of China, 2011, 21(8): 1817−1825.

[10] WENK H R, CANOVA G, BRECHET Y, FLANDIN L. A deformation-based model for recrystallization of anisotropic materials [J]. Acta Materialia, 1997, 45(8): 3283−3296.

[11] PÉREZ-PRADO M T, RUANO O A. Texture evolution during annealing of magnesium AZ31 alloy [J]. Scripta materialia, 2002, 46(2): 149−155.

[12] WALDE T, RIEDEL H. Modeling texture evolution during hot rolling of magnesium alloy AZ31 [J]. Materials Science and Engineering A, 2007, 443(1): 277−284.

[13] GOTTSTEIN G, AL SAMMAN T. Texture development in pure Mg and Mg alloy AZ31 [J]. Materials Science Forum, 2005, 495−497:

623−632.
[14] WU B, WAN G, ZHANG Y, DU X, WAGNER F, ESLING C. Fragmentation of large grains in AZ31 magnesium alloy during ECAE via route A [J]. Materials Science and Engineering A, 2010, 527(15): 3365−3372.
[15] OSTAPOVETS A, MOLNÁR P, JÄGER A. Visco-plastic self-consistent modelling of a grain boundary misorientation distribution after equal-channel angular pressing in an AZ31 magnesium alloy [J]. Journal of Materials Science, 2013, 48(5): 2123−2134.
[16] LEBENSOHN R A, TOMÉ C N. A self-consistent anisotropic approach for the simulation of plastic deformation and texture development of polycrystals: Application to zirconium alloys [J]. Acta Metallurgica et Materialia, 1993, 41(9): 2611−2624.
[17] ESHELBY J D. The determination of the elastic field of an ellipsoidal inclusion, and related problems [C]//Proceedings of the Royal Society of London A. London: The Royal Society, 1957, 241(1226): 376−396.
[18] TOMÉ C N, LEBENSOHN R A, KOCKS U F. A model for texture development dominated by deformation twinning: Application to zirconium alloys [J]. Acta Metallurgica et Materialia, 1991, 39(11): 2667−2680.
[19] AGNEW S R, YOO M H, TOMÉ C N. Application of texture simulation to understanding mechanical behavior of Mg and solid solution alloys containing Li or Y [J]. Acta Materialia, 2001, 49(20): 4277−4289.
[20] SITDIKOV O, KAIBYSHEV R. Dynamic Recrystallization in pure magnesium [J]. Materials Transactions, 2001, 42(9): 1928−1937.
[21] SHAO Yi-chuan, TANG Tao, LI Da-yong, TANG Wei-qin, PENG Ying-hong. Crystal plasticity finite element modelling of the extrusion texture of a magnesium alloy [J]. Modelling and Simulation in Materials Science and Engineering, 2015, 23(5): 055011.
[22] QUAN Guo-zheng, SHI Yu, WANG Yi-xin, KANG Beom-soo, KU Tae-wan, SONG Woo-jin. Constitutive modeling for the dynamic recrystallization evolution of AZ80 magnesium alloy based on stress–strain data [J]. Materials Science and Engineering A, 2011, 528(28): 8051−8059.
[23] POLIAK E I, JONAS J J. A one-parameter approach to determining the critical conditions for the initiation of dynamic recrystallization [J]. Acta Materialia, 1996, 44(1): 127−136.
[24] JAIN A, AGNEW S R. Modeling the temperature dependent effect of twinning on the behavior of magnesium alloy AZ31B sheet [J]. Materials Science and Engineering A, 2007, 462(1): 29−36.
[25] BARNETT M R. A Taylor model based description of the proof stress of magnesium AZ31 during hot working [J]. Metallurgical and Materials Transactions A, 2003, 34(9): 1799−1806.
[26] HERNANDEZ C A, MEDINA S F, RUIZ J. Modelling austenite flow curves in low alloy and microalloyed steels [J]. Acta Materialia, 1996, 44(1): 155−163.
[27] JIN L, MISHRA R K, SACHDEV A K. Texture modification during extrusion of some Mg alloys [J]. Metallurgical and Materials Transactions A, 2012, 43(6): 2148−2157.
[28] MISHRA R K, GUPTA A K, RAO P R, SACHDEV A K, KUMAR A M, LUO A A. Influence of cerium on the texture and ductility of magnesium extrusions [J]. Scripta Materialia, 2008, 59(5): 562−565.

AZ80 镁合金热挤压织构的多晶体建模

邵一川，汤 韬，李大永，周国伟，张少睿，彭颖红

上海交通大学 机械与动力工程学院 机械系统与振动国家重点实验室，上海 200240

摘 要：为合理模拟 AZ80 镁合金的热挤压织构，在粘塑性自洽(VPSC)多晶体塑性框架中实现了动态再结晶织构的模拟。基于此模型，考察了挤压温度和挤压边界条件对 AZ80 镁合金挤压织构的影响，模拟所得结果与实验结果有较好的吻合。模拟结果表明：新的大角度界面(HABs)的形成使再结晶晶粒与母晶之间形成取向差，再结晶晶粒因此偏离母晶形成了 $\{2\bar{1}\bar{1}0\}$ 纤维织构组分。此外，因为基面⟨*a*⟩滑移具有更低的滑移抗力并易于开动，当垂直于挤压轴方向上加载的应变不再轴对称时，晶粒的基面总倾向于转向加载应变更多的方向以便于基面⟨*a*⟩滑移承载更多的塑性变形。挤压温度的升高有利于锥面⟨*c*+*a*⟩滑移的开动并使再结晶体积分数增多，在一定程度上弱化了挤压形成的基面织构。

关键词：AZ80 镁合金；多晶体塑性；织构；热挤压；动态再结晶

(Edited by Mu-lan QIN)